# $\rho$-meson spectroscopy and diffractive production using the holographic light-front Schrödinger equation and the 't Hooft equation

Bheemsehan Gurjar,[1,*] Chandan Mondal,[2,3,†] and Satvir Kaur[2,3,‡]

[1]*Department of Physics, Indian Institute of Technology Kanpur, Kanpur-208016, India*
[2]*Institute of Modern Physics, Chinese Academy of Sciences, Lanzhou 730000, China*
[3]*School of Nuclear Science and Technology, University of Chinese Academy of Sciences, Beijing 100049, China*

(Received 29 January 2024; accepted 9 April 2024; published 10 May 2024)

We determine the mass spectroscopy and light-front wave functions (LFWFs) of the $\rho$-meson by solving the holographic Schrödinger equation of light-front chiral QCD along with the 't Hooft equation of $(1+1)$-dimensional QCD in the large $N_c$ limit. Subsequently, we utilize the obtained LFWFs in conjunction with the color glass condensate dipole cross section to calculate the cross sections for the diffractive $\rho$-meson electroproduction. Our spectroscopic results align well with the experimental data. Predictions for the diffractive cross sections demonstrate good consistency with the available experimental data at different energies from H1 and ZEUS collaborations. Additionally, we show that the resulting LFWFs for the $\rho$-meson can effectively describe various properties, including its decay constant, distribution amplitudes, electromagnetic form factors, charge radius, magnetic and quadrupole moments. Comparative analyses are conducted with experimental measurements and the available theoretical predictions.

DOI: 10.1103/PhysRevD.109.094017

## I. INTRODUCTION

Experimental processes such as deep inelastic scattering (DIS), deeply virtual Compton scattering (DVCS), and exclusive diffractive vector meson production serve as effective tools to investigate quantum chromodynamics (QCD) [1]. Particularly, at small $x$, these processes are predominantly influenced by gluon saturation. This phenomenon has extensively been explored within the framework of the color glass condensate (CGC) effective field theory [2–6]. The CGC theory describes the balance of gluons through recombination and multiple scattering limitations within a dipole picture [7–10]. In this dipole model, a virtual photon splits into a quark and an antiquark pair (dipole), interacts with proton through gluon exchange, and reforms into a vector meson or photon as illustrated in Fig. 1.

The goal of this paper is to predict the cross section for diffractive $\rho$-meson electroproduction, observed at the HERA collider [11–16], using the QCD color dipole model and the nonperturbative holographic meson LFWFs [17] by taking into account the longitudinal dynamics generated by the 't Hooft equation in $(1+1)$-dim QCD at large $N_c$ [18].

The holographic light-front QCD (hLFQCD) is developed within the chiral limit of light-front QCD, establishing an exact correspondence between strongly coupled $(1+3)$-dimensional light-front QCD and weakly interacting string modes in $(1+4)$-dimensional anti-de-Sitter (AdS) space. For a review of hLFQCD, see Ref. [19]. The primary nontrivial prediction of this approach leads to the lightest bound state, i.e., the pion is massless. Another crucial prediction asserts that the meson masses align along the universal Regge trajectories, mirroring experimental observations. Note that the predicted slopes are dictated by the strength of the confining potential, $\kappa$. The form of the confining potential in physical spacetime is determined by a dilaton field that breaks the conformal symmetry of AdS space. A phenomenologically successful choice involves a quadratic dilaton in the fifth dimension of AdS space, which corresponds to a light-front harmonic oscillator in physical spacetime. The mass scale parameter, $\kappa$, is fixed by fitting the experimentally observed slopes of the meson mass spectrum Regge trajectories for different meson groups. It is found that for all the light mesons, $\kappa \simeq 0.5$ GeV [17].

Going beyond the semiclassical approximation, Brodsky and de Téramond (BdT) proposed an invariant mass ansatz (IMA) for including nonzero quark masses [20]. Using IMA, one can calculate the shift in the meson masses as a

*gbheem@iitk.ac.in
†mondal@impcas.ac.cn
‡satvir@impcas.ac.cn

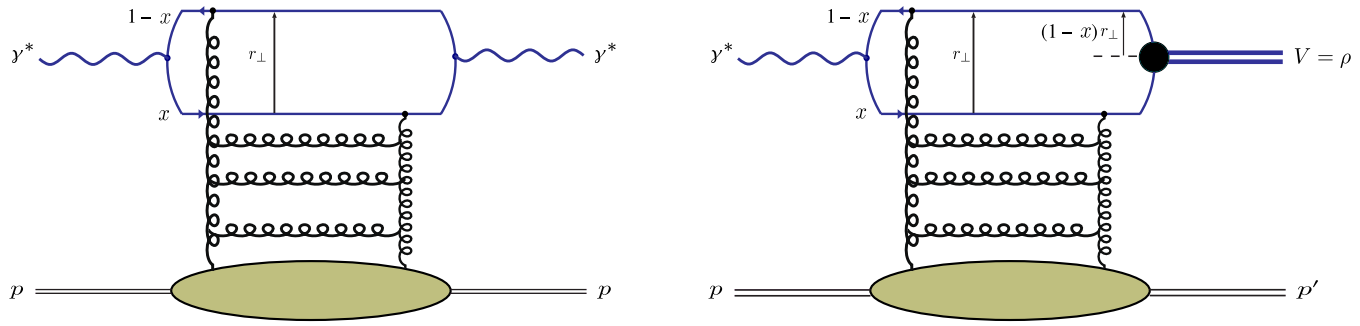


FIG. 1. The $\gamma^* p$ elastic scattering amplitude for DIS (left) and for exclusive vector meson production (right) in dipole model. Here, $x$ is the fraction of the photon momentum carried by the quark and $\mathbf{r}_\perp$ is the transverse size of the dipole.

first order perturbation. The predicted mass shift for the pion (and kaon) appears as same as the physical mass of the meson. These results have been obtained by fixing the scale parameter as $\kappa = 0.54$ GeV, and the light quark masses as $m_{u/d} = 0.046$ GeV and $m_s = 0.357$ GeV, which vanish in the chiral limit [17].

Previous works [21,22] reported predictions for vector mesons production by utilizing the holographic wave function with IMA together with the CGC dipole cross section [23]. Reference [21] has investigated the process of $\rho$-meson production using a light quark mass of $m_q = 0.14$ GeV, which is consistent with the fitted parameters of CGC dipole cross section [24,25] from the inclusive DIS data [26,27]. The most recent analyses of dipole cross sections have utilized the 2010 DIS data at HERA [28]. It has been acknowledged in Ref. [23] that the DIS data prefers the lower light quark masses, but also noted that the use of effective quark mass, $m_q = 0.14$ GeV, yields satisfactory fit to the 2001 DIS structure function data. In a more recent study [29], a novel dipole model has demonstrated that both current quark mass and effective quark mass $m_q = 0.14$ GeV accurately fit the 2010 DIS structure function data [28]. In Ref. [22], the authors revisited the CGC dipole model and fit the conclusive 2015 HERA data of inclusive DIS with the light quark masses. They studied cross sections for the diffractive $\rho$ and $\phi$ meson production using the fitted dipole cross section [30], the perturbatively calculated photon LFWFs [31,32], and the holographic meson LFWFs with IMA, which contains no dynamical information of the meson in the longitudinal direction [33].

In this work, the nonzero light quark masses are incorporated through the chiral symmetry breaking and the longitudinal dynamics governed by the 't Hooft equation of $(1+1)$-dimensional QCD in the large $N_c$ limit. The combined holographic Schrödinger equation and the 't Hooft equation provide a reliable picture of the data to the $\rho$-meson spectrum with the universal $\kappa$. We show that, together, they can simultaneously describe various properties of the $\rho$-meson, including its decay constant, parton distribution amplitude (PDA), electromagnetic form factors, charge radius etc., as well as, in conjunction with the CGC dipole cross section, the resulting wave functions can provide good description of the HERA data of the diffractive $\rho$-meson electroproduction.

The rest of the paper is organized as follows: In Sec. II, we review the color dipole model. The holographic meson LFWFs followed by the longitudinal dynamics using the 't Hooft equation are discussed in Sec. III. In Sec. IV, we discuss the numerical results for the mass spectroscopy, the diffractive cross sections using the dipole cross section, PDAs, electromagnetic form factors, decay constant, charge radius, magnetic and quadrupole moments for the $\rho$-meson with the holographic meson wave function. Finally, we conclude the paper in Sec. V.

## II. THE DIPOLE MODEL OF EXCLUSIVE VECTOR MESON PRODUCTION

In the dipole picture, the scattering amplitude for the diffractive process $\gamma^* p \to Vp$ is expressed as the convolution of the overlap of the LFWFs of the photon and the vector meson, and the proton-dipole scattering amplitude [24],

$$\Im\mathrm{m}\mathcal{A}_\Lambda^{\gamma^* p\to Vp}(s,t;Q^2) = \sum_{h,\bar{h}} \int \mathrm{d}^2\mathbf{r}_\perp \,\mathrm{d}x \Psi_{h,\bar{h}}^{\gamma^*,\Lambda}(x,\mathbf{r}_\perp;Q^2) \times \Psi_{h,\bar{h}}^{V,\Lambda}(x,\mathbf{r}_\perp)^* e^{-ix\mathbf{r}_\perp\cdot\boldsymbol{\Delta}} \mathcal{N}(x_\mathrm{m},\mathbf{r}_\perp,\boldsymbol{\Delta}), \tag{1}$$

where $Q^2$ is the virtuality of the photon and $t = -\Delta^2$ is the squared of the transverse momentum transfer at the proton vertex. The substantial value of the center-of-mass energy squared, $s$, ensures the factorization of the scattering amplitude for the diffractive process into a convolution of the LFWFs of the photon, $\Psi_{h,\bar{h}}^{\gamma,\Lambda}(x,\mathbf{r}_\perp;Q^2)$, and vector meson, $\Psi_{h,\bar{h}}^{V,\Lambda}(x,\mathbf{r}_\perp)$, and a dipole cross section, $\mathcal{N}(x_\mathrm{m},\mathbf{r}_\perp,\Delta)$. The variable $\mathbf{r}_\perp$ is the transverse size of the dipole and $x$ defines the longitudinal momentum fraction carried by the quark as shown in Fig. 1. The indices $h$ and $\bar{h}$

are the helicities of the quark and the antiquark. The symbol $\Lambda$ in the superscript of the LFWFs denotes the polarization of the photon and the vector meson. The systems can be longitudinally polarized or transversely polarized; symbolically, $\Lambda = 0$ or $\pm 1$, respectively. The dipole-proton scattering amplitude depends upon the center-of-mass energy of the photon-proton system ($W$), related to the modified Bjorken variable as [34]: $x_{\rm m} = x_{\rm Bj}(1 + \frac{M_V^2}{Q^2})$, where $x_{\rm Bj} = \frac{Q^2}{W^2}$. The dipole-proton scattering amplitude encapsulates the high-energy QCD dynamics associated with the dipole-proton interaction. Being a universal object, it can be obtained via an approximate solution of the Balitsky-Kovchegov equation [35–37] within the CGC formalism [38–42].

The differential cross section for the exclusive vector meson production is given by [15,23],

$$\frac{d\sigma_\Lambda^{\gamma^* p\to Vp}}{dt} = \frac{1}{16\pi}[\Im\mathrm{m}\mathcal{A}_\Lambda^{\gamma^* p\to Vp}(s, t=0)]^2 \times (1+\beta_\Lambda^2)\exp(-B_D t) \tag{2}$$

with the parameter $\beta_\Lambda$ being the ratio of the real to imaginary components of the scattering amplitude expressed as [23,43],

$$\beta_\Lambda = \tan\left(\frac{\pi}{2}\alpha_\Lambda\right) \quad \text{with} \quad \alpha_\Lambda = \frac{\partial \log|\Im\mathrm{m}\mathcal{A}_\Lambda|}{\partial \log(1/x_{\rm m})}, \tag{3}$$

and the diffractive slope parameter $B_D$ parametrized as [22],

$$B_D = N\left[14.0\left(\frac{1\ \mathrm{GeV}^2}{Q^2+M_V^2}\right)^{0.2} + 1\right] \tag{4}$$

with $N = 0.55\ \mathrm{GeV}^{-2}$. The parametrization of this slope parameter is consistent with the ZEUS data for $\rho$-meson production [15,43]. However, the most recent H1 data [12] favors somewhat larger value of $B_D$ accompanied by the large uncertainty.

A simplified model for the dipole cross section was proposed a long ago in Ref. [30], known as the CGC dipole model. The dipole cross section is given by

$$\hat{\sigma}(x_{\rm m}, r_\perp) = \sigma_0 \mathcal{N}(x_{\rm m}, r_\perp Q_s, 0) \tag{5}$$

with

$$\mathcal{N}(x_{\rm m}, r_\perp Q_s, 0) = \begin{cases} \mathcal{N}_0\left(\frac{r_\perp Q_s}{2}\right)^{2\left[\gamma_s + \frac{\ln(2/r_\perp Q_s)}{\kappa_0 \lambda \ln(1/x_{\rm m})}\right]} & \text{for } r_\perp Q_s \le 2, \\ 1 - \exp[-\mathcal{A}\ln^2(\mathcal{B} r_\perp Q_s)] & \text{for } r_\perp Q_s > 2 \end{cases} \tag{6}$$

where $r_\perp = |\mathbf{r}_\perp|$ and the saturation scale is $Q_s = (x_0/x_{\rm m})^{\lambda/2}$ GeV. The coefficients $\mathcal{A}$ and $\mathcal{B}$ in Eq. (6) are determined uniquely from the condition that $\mathcal{N}(x_{\rm m}, r_\perp Q_s, 0)$ and its derivative with respect to $r_\perp Q_s$ are continuous at $r_\perp Q_s = 2$. This leads to

$$\mathcal{A} = -\frac{\mathcal{N}_0^2 \gamma_s^2}{(1-\mathcal{N}_0)^2 \ln(1-\mathcal{N}_0)}, \quad \mathcal{B} = \frac{1}{2}(1-\mathcal{N}_0)^{-\frac{(1-\mathcal{N}_0)}{\mathcal{N}_0 \gamma_s}}. \tag{7}$$

The free parameters of the CGC dipole model, $\sigma_0, \lambda, x_0$, and $\gamma_s$ are determined by a fit to the H1 and ZEUS (2015) $F_2$ structure function data [44] (for $x_{\rm Bj} \le 0.01$ and $Q^2 \in [0.045, 45]\ \mathrm{GeV}^2$) with a $\chi^2/\mathrm{d.o.f} = 1.03$ [22]. Here, we use the parameters as determined in Ref. [22] as: $\sigma_0 = 26.3$ mb, $\gamma_s = 0.741, \lambda = 0.219$, and $x_0 = 1.81 \times 10^{-5}$ for $m_{u,d} \sim 0.046$ GeV. The parameters $\mathcal{N}_0$ and $\kappa_0$ are fixed as 0.7 and 9.9 (leading order Balitsky-Fadin-Kuraev-Lipatov prediction), respectively.

To compute the scattering amplitude for exclusive $\rho$-meson production, Eq. (1), we need to employ the LFWFs of the incoming virtual photon and the outgoing vector meson. In practice, the expressions for the photon LFWFs are obtained perturbatively in light-front QED. The lowest order perturbative LFWFs for the longitudinally and transversely polarized photons are given by [31,32,45],

$$\begin{aligned}\Psi_{h,\bar{h}}^{\gamma,\Lambda=0}(x, \mathbf{r}_\perp; Q^2, m_q) &= \sqrt{\frac{N_c}{4\pi}}\delta_{h,-\bar{h}} e e_q 2x(1-x) \times Q\frac{K_0(\epsilon \mathbf{r}_\perp)}{2\pi}, \\ \Psi_{h,\bar{h}}^{\gamma,\Lambda=\pm 1}(x, \mathbf{r}_\perp; Q^2, m_q) &= \pm\sqrt{\frac{N_c}{2\pi}} e e_q [i e^{\pm i\theta_{\mathbf{r}_\perp}}(x\delta_{h\pm,\bar{h}\mp} \\ &\quad - (1-x)\delta_{h\mp,\bar{h}\pm})\partial_{\mathbf{r}_\perp} \\ &\quad + m_q \delta_{h\pm,\bar{h}\pm}]\frac{K_0(\epsilon \mathbf{r}_\perp)}{2\pi},\end{aligned} \tag{8}$$

where $\epsilon^2 = x(1-x)Q^2 + m_q^2$ and $e^2 = 4\pi\alpha_{\rm em}$ with $\alpha_{\rm em}$ being the QED coupling constant, $e_q$ and $m_q$ represent the effective charge and mass of the quark, respectively. $N_c$ corresponds to the color factor, $K_0$ denotes the second kind of Bessel function and $r_\perp e^{i\theta_{\mathbf{r}_\perp}}$ is the complex notation for the transverse distance between the quark and the antiquark. On the other hand, a nonperturbative model for the meson LFWFs is discussed in Sec. III.

The total cross section is expressed as the linear combination of the transverse and longitudinal cross sections by integrating them (given in Eq. (2)) over $t$. Therefore,

$$\sigma_{\rm tot}^{\gamma^* p\to Vp}(x, Q^2) = \sigma_{\Lambda=\pm 1}^{\gamma^* p\to Vp}(x, Q^2) + \varepsilon\sigma_{\Lambda=0}^{\gamma^* p\to Vp}(x, Q^2), \tag{9}$$

where $\varepsilon$ is the photon polarization parameter, with $\langle\varepsilon\rangle = 0.98$ in the kinematic domain corresponding to the HERA

measurement for the $\rho$-meson production [12]. We consider the same value of $\varepsilon$ for predicting the total cross section and compare it with the HERA data.

## III. HOLOGRAPHIC MESON WAVE FUNCTIONS WITH LONGITUDINAL CONFINEMENT

In the previous section, we reviewed the photon wave functions, which are obtained from the perturbative QED. The vector meson LFWFs appearing in Eq. (1) cannot be obtained in perturbation theory. Nevertheless, they can be considered to have the same spinor and polarization structure as in the photon case, together with an unidentified nonperturbative wave function. Various ansatz for the meson nonperturbative wave functions have been reported in literature [8,21,32]. However, the most popular is the boosted Gaussian wave function [8,46], which has recently been employed in Refs. [43,47] to simultaneously reproduce the cross-section data for diffractive $\rho, \phi$ and $J/\Psi$ production. Explicitly, the spin-improved LFWFs for longitudinally and transversely polarized vector meson can be written as [21,46,48,49]

$$\Psi^{V,\Lambda=0}_{h,\bar{h}}(x,\mathbf{r}_\perp) = \frac{1}{2}\delta_{h,-\bar{h}}\left[1+\frac{m_q^2-\nabla^2_{\mathbf{r}_\perp}}{x(1-x)M_V^2}\right]\Psi(x,\mathbf{r}_\perp), \quad (10)$$

and

$$\Psi^{V,\Lambda=\pm1}_{h,\bar{h}}(x,\mathbf{r}_\perp) = \pm[ie^{\pm i\theta_{\mathbf{r}_\perp}}(x\delta_{h\pm,\bar{h}\mp}-(1-x)\delta_{h\mp,\bar{h}\pm})\partial_{\mathbf{r}_\perp} + m_q\delta_{h\pm,\bar{h}\pm}]\frac{\Psi(x,\mathbf{r}_\perp)}{2x(1-x)}, \quad (11)$$

respectively, where $\Psi$ represents the spin independent part of the vector meson wave functions.

Brodsky and de Téramond proposed a nonperturbative approach to construct the hadronic LFWFs based on hLFQCD [33,50,51]. To connect with AdS space, a holographic variable, $\zeta = \sqrt{x(1-x)}r_\perp$ is introduced, and the wave function is written in a factorized form in terms of $x$, $\zeta$, and $\varphi$ variables:

$$\Psi(x,\zeta,\varphi) = \frac{\phi(\zeta)}{\sqrt{2\pi\zeta}}e^{iL\varphi}X(x), \quad (12)$$

where $X(x) = \sqrt{x(1-x)}\chi(x)$ and $\phi(\zeta)$ are referred as the longitudinal and transverse modes, respectively and $L$ is the orbital quantum number. In hLFQCD, only the transverse mode, $\phi(\zeta)$, is dynamical and it is generated by the holographic Schrödinger-like equation [19,52–54],

$$\left(-\frac{d^2}{d\zeta^2}+\frac{4L^2-1}{4\zeta^2}+U_\perp(\zeta)\right)\phi(\zeta) = M_\perp^2\phi(\zeta), \quad (13)$$

where the confinement potential is given by

$$U_\perp(\zeta) = \kappa^4\zeta^2 + 2\kappa^2(J-1), \quad (14)$$

with $J = L + S$ being the total angular momentum of the meson. The analytical expression of Eq. (14) is uniquely determined by a holographic mapping to $AdS_5$, where light-front variable $\zeta$ maps onto the fifth dimension of AdS space and the underlying conformal symmetry [55]. The emerging mass scale, $\kappa$, fixes the confinement scale and produces meson masses in the chiral limit. Using Eq. (14) in Eq. (13) yields

$$M_\perp^2(n_\perp, J, L) = 4\kappa^2\left(n_\perp + \frac{J+L}{2}\right), \quad (15)$$

and

$$\phi_{n_\perp L}(\zeta) \propto \zeta^{1/2+L}\exp\left(\frac{-\kappa^2\zeta^2}{2}\right)L^L_{n_\perp}(\kappa^2\zeta^2), \quad (16)$$

with $n_\perp$ being the transverse principle quantum number. An important outcome of Eq. (15) is that the lowest-lying hadronic bound state, with $n_\perp = L = S = 0$, is massless. This is inherently recognized as the pion, which is anticipated to exhibit zero mass in the chiral limit of QCD.

Meanwhile, the longitudinal mode, $\chi(x)$, is not dynamical in hLFQCD. The longitudinal wave function, $X(x) = \sqrt{x(1-x)}$ is explicitly obtained by the holographic mapping of the electromagnetic or gravitational form factor in physical spacetime and $AdS_5$ [56,57]. This results $\chi(x) = 1$. Inserting Eq. (16) in Eq. (12) yields the holographic LFWFs in the chiral-limit. For the ground state mesons ($n_\perp = 0, L = 0$), the holographic LFWFs become

$$\Psi_{m_q=0}(x,\zeta^2) \propto \sqrt{x(1-x)}\exp\left(\frac{-\kappa^2\zeta^2}{2}\right). \quad (17)$$

A two-dimensional Fourier transform results

$$\Phi_{m_q=0}(x,k_\perp^2) \propto \frac{1}{\sqrt{x(1-x)}}\exp\left(-\frac{k_\perp^2}{2\kappa^2x(1-x)}\right), \quad (18)$$

where $k_\perp = |\mathbf{k}_\perp|$, the Fourier conjugate of $\mathbf{r}_\perp$, defines the transverse momentum of the quark. Going beyond the chiral limit, Brodsky and de Téramond proposed a prescription to describe the longitudinal mode as [20]:

$$X(x) = \sqrt{x(1-x)}\exp\left[-\frac{1}{2\kappa^2}\left(\frac{m_q^2}{x}+\frac{m_{\bar{q}}^2}{1-x}\right)\right], \quad (19)$$

based on the observation that the chiral-limit of invariant mass of quark-antiquark pair,

$$\mathcal{M}^2_{q\bar{q}} = \frac{k_\perp^2}{x(1-x)}+\frac{m_q^2}{x}+\frac{m_{\bar{q}}^2}{1-x}, \quad (20)$$

appears in Eq. (18). Consequently, the bound-state mass eigenvalue receives a first-order correction such that

$$\Delta M^2 = \int \frac{\mathrm{d}x}{x(1-x)} X^2(x) \left( \frac{m_q^2}{x} + \frac{m_{\bar{q}}^2}{1-x} \right). \tag{21}$$

Note that there are two shortcomings with the above prescription. First, it indicates that [58] $M_\pi^2 = \Delta M^2 \propto 2m_q^2(\ln(\kappa^2/m_q^2) - \gamma_E)$ with $\gamma_E = 0.577216$ being the Euler's constant, in contrast to the Gell-Mann-Oakes-Renner (GMOR) relation, $M_\pi^2 \propto m_q$. Second, the longitudinal mode, given by Eq. (19), with no nodes, remains same for all the radially excited states. However, this prescription has successfully been implemented to describe the light as well as heavy mesons [19,20,59–65].

It has been reported in Ref. [59] that, in practice, the longitudinal dynamics can be included by performing an expansion of the IMA longitudinal mode, Eq. (19), using the convenient basis of complete orthonormal eigenfunctions generated by the effective potential [66]

$$U_\parallel(x) = -\sigma^2 \frac{d}{dx} \left( x(1-x) \frac{d}{dx} \right), \tag{22}$$

with $\sigma$ being the strength of the potential. The longitudinal mode can be expressed as,

$$X(x) = \sqrt{x(1-x)}\chi_{\mathrm{IMA}}(x) = \sqrt{x(1-x)} \sum_i C_i \chi_i(x), \tag{23}$$

where $\chi_i(x)$, the solution of the longitudinal dynamical equation with the effective potential $U_\parallel(x)$, is given by

$$\chi_i(x) = N x^{\alpha/2} (1-x)^{\beta/2} P_i^{(\alpha,\beta)}(1-2x), \tag{24}$$

with $\alpha = 2m_q/\sigma$, $\beta = 2m_{\bar{q}}/\sigma$. $P_i^{(\alpha,\beta)}$ represents a Jacobi polynomial of order $i$, and $N$ is a normalization constant. The expansion coefficients $C_i$ are obtained from the overlap

$$C_i = \int_0^1 \mathrm{d}x \chi_i(x) \chi_{\mathrm{IMA}}(x), \tag{25}$$

with $\langle \chi_{\mathrm{IMA}} | \chi_{\mathrm{IMA}} \rangle = \sum_i C_i^2 = 1$. The corresponding longitudinal contribution to a meson mass is given by [59]

$$M_\parallel^2 = (m_q + m_{\bar{q}})^2 + \sigma(m_q + m_{\bar{q}}) + \sum_{i=1}^{\infty} C_i^2 [(2i\sigma(m_q + m_{\bar{q}}) + i(i+1)\sigma^2]. \tag{26}$$

Meanwhile, Refs. [67,68] consider longitudinal dynamics, generated by the 't Hooft equation, in order to describe the full meson spectrum, while the pion dynamics has been predicted in Ref. [69]. The concept of employing the 't Hooft equation to extend beyond the invariant mass prescription was initially suggested in Ref. [70], aiming to forecast meson decay constants and parton distribution functions. Recently, in Refs. [58,59], the prescription was surpassed using a phenomenological longitudinal confinement potential, which was initially introduced in Ref. [66] within the framework of basis light-front quantization. While both Refs. [58,59] concentrate on the chiral limit and the occurrence of chiral symmetry breaking, Ref. [59] broadens their investigation to heavy mesons in their ground state and explores the connection of their approach to the 't Hooft equation. It is worth mentioning that there has been a notable surge in interest regarding the incorporation of longitudinal dynamics within hLFQCD [58,59,67,71–73]. Recently, in Ref. [74], the authors reported the production of diffractive J/Ψ and Ψ(2S) mesons using the hLFQCD framework, incorporating longitudinal dynamics with the 't Hooft model.

The 't Hooft equation can be derived by using the QCD Lagrangian in $(1+1)$-dim with large $N_c$ approximations as [18]

$$\left( \frac{m_q^2}{x} + \frac{m_{\bar{q}}^2}{1-x} \right) \chi(x) + \frac{g^2}{\pi} \mathcal{P} \int \mathrm{d}y \frac{\chi(x) - \chi(y)}{(x-y)^2} = M_\parallel^2 \chi(x), \tag{27}$$

where $g$ is the longitudinal confinement scale and $\mathcal{P}$ denotes the Cauchy principal value. It is important to note that in the conformal limit, the 't Hooft equation has a gravity dual on $AdS_3$ [75] and has been widely studied in the literature [67,69,76–82]. Unlike the holographic light-front Schrödinger equation, the 't Hooft does not admit analytical solutions. We solve it numerically using the matrix method illustrated in Ref. [70]. Using both the holographic Schrödinger equation and the 't Hooft equation, the meson mass is then given by

$$M^2(n_\perp, n_\parallel, J, L) = 4\kappa^2 \left( n_\perp + \frac{J+L}{2} \right) + M_\parallel^2(n_\parallel, m_q, m_{\bar{q}}, g), \tag{28}$$

where $n_\parallel$ defines the longitudinal quantum number. Since, the holographic Schrödinger equation predicts a massless pion, it follows that the only contribution to the pion mass is produced by the 't Hooft equation. Note that together, the holographic Schrödinger equation and the 't Hooft equation correctly predict the GMOR relation $M_\pi^2 \sim m_{u,d}$ [59,69]. With the universal transverse confinement scale $\kappa = 0.523$ GeV and the light quark mass $m_{u/d} = 0.046$ GeV, which is the value considered in hLFQCD together with the IMA [19], the longitudinal confining scale $g = 0.109$ GeV leads to excellent agreement of the mass spectroscopy for the pion family with the experimental data [69]. In this work, we use the same set of parameters in order to predict

the spectroscopic data for the $\rho$-meson family and obtain the corresponding wave functions.

The complete spin-independent part of the meson LFWFs can then be expressed as,

$$\Psi(x,\zeta) = \mathcal{N}\sqrt{x(1-x)}\chi(x)\exp\left[-\frac{\kappa^2\zeta^2}{2}\right], \quad (29)$$

where $\chi(x)$ is the solution of the 't Hooft equation. $\mathcal{N}$ is a normalization constant, which depends on polarization of the meson and can be fixed by using the normalization condition as,

$$\sum_{h,\bar{h}}\int \mathrm{d}^2\mathbf{r}_\perp \mathrm{d}x|\Psi^{V,\Lambda}_{h,\bar{h}}(x,\mathbf{r}_\perp)|^2 = 1, \quad (30)$$

where the forms of the spin-improved wave functions $\Psi^{V,\Lambda}_{h,\bar{h}}$ are given in Eqs. (10) and (11). The numerical solutions for the longitudinal modes $\chi(x)$ of the ground state meson can approximately be fitted to the following polynomial form:

$$\chi(x) \simeq x^{\beta_1}(1-x)^{\beta_2}, \quad (31)$$

with $\beta_i$ being the quark mass dependent variables, which vanish in the chiral limit. For the ground state of $\rho$-meson, we find that $\beta_{1,2} = 0.51$.

## IV. RESULTS AND DISCUSSION

### A. Mass spectroscopy and longitudinal mode

The parity and charge conjugation quantum numbers of meson states are given by [67–69]:

$$P = (-1)^{L+1}, \qquad C = (-1)^{L+S+n_\parallel}. \quad (32)$$

Using Eq. (28) and the parameters determined for the pion family: $m_{u/d} = 0.046$ GeV, $\kappa = 0.523$ GeV, and $g = 0.109$ GeV [69], we are able to describe the spectroscopic data for the $\rho$-meson family. We present our computed masses of the $\rho$-meson and its excited states in Table I. Our results (last column) are in good agreement with the experimental data (second column, in parentheses). Note that an emerging condition $n_\parallel \geq n_\perp + L$ in Table I is observed to remain true across the full hadron spectrum [68]. The resulting Regge trajectories for the $\rho$-meson family in our calculation are shown in Fig. 2.

TABLE I. Quantum numbers and masses of the $\rho$-meson family with $S = 1$. $M_\perp$ and $M_\parallel$ are obtained by solving the transverse and longitudinal dynamical equations, the holographic Schrödinger equation and the 't Hooft equation, respectively.

| $J^{P(C)}$ | Name | $n_\perp$ | $n_\parallel$ | $L$ | $M_\parallel$ [MeV] | $M_\perp$ [MeV] | $M_{\rm tot}$ [MeV] (This work) |
|---|---|---|---|---|---|---|---|
| $1^{--}$ | $\rho(770)$ | 0 | 0 | 0 | 134 | 740 | 752 |
| $2^{++}$ | $a_2(1320)$ | 0 | 2 | 1 | 296 | 1281 | 1315 |
| $3^{--}$ | $\rho_3(1690)$ | 0 | 4 | 2 | 401 | 1654 | 1702 |
| $4^{++}$ | $a_4(1970)$ | 0 | 6 | 3 | 484 | 1957 | 2016 |
| $1^{--}$ | $\rho(1450)$ | 1 | 2 | 0 | 296 | 1281 | 1315 |
| $2^{++}$ | $a_2(1700)$ | 1 | 4 | 1 | 401 | 1654 | 1702 |
| $1^{--}$ | $\rho(1700)$ | 2 | 4 | 0 | 401 | 1654 | 1702 |

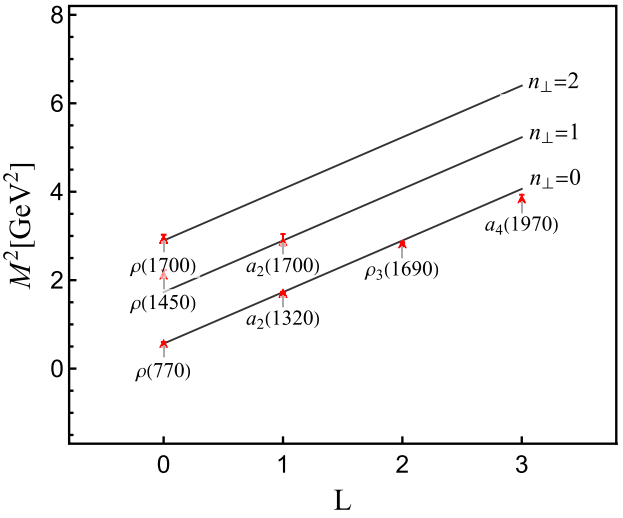


FIG. 2. Our Regge trajectories for the $\rho$-meson family.

Figure 3 shows our numerical results for the dynamical longitudinal mode of the ground-state meson ($u\bar{d}$) compared to those outlined in Ref. [59], Eq. (23), and the IMA. Note that the effective quark mass employed in our calculations and in the IMA is $m_q = 46$ MeV, while a different quark mass, $m_q = 28$ MeV, has been considered

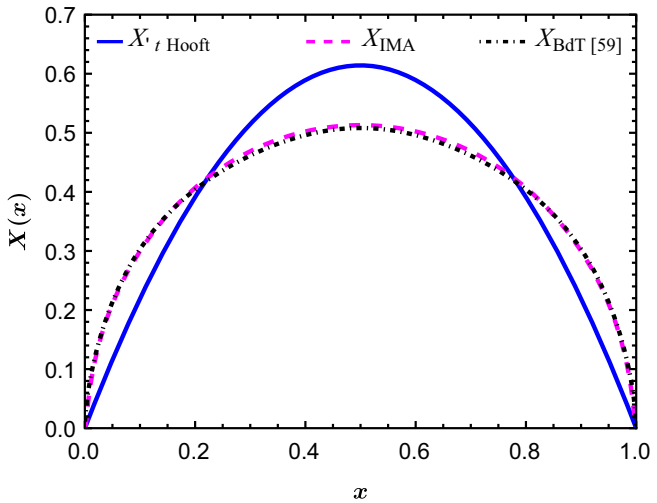


FIG. 3. Comparison of the longitudinal mode of the light meson ($u\bar{d}$). The longitudinal mode obtained by solving the 't Hooft equation (blue-solid line) is compared with that outlined in Ref. [59] (referred as BdT) (black-dash-dotted line) and the IMA (magenta-dashed line).

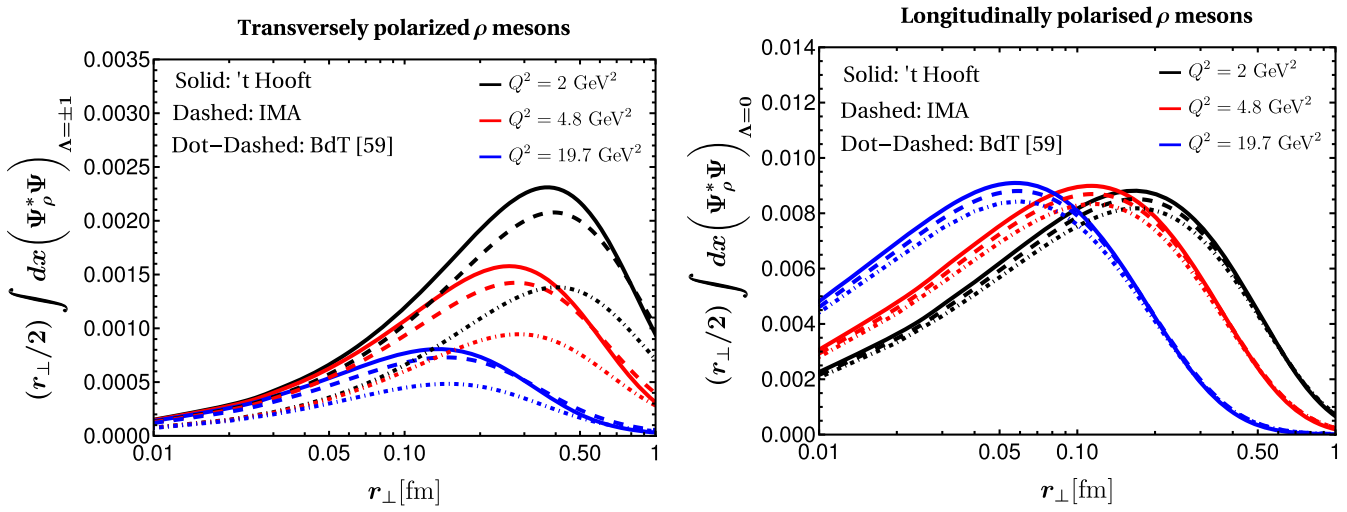


FIG. 4. The transverse (left) and the longitudinal (right) overlap functions between the photon and the $\rho$-meson LFWFs integrated over $x$ as a function of the dipole transverse size $\mathbf{r}_\perp$ (in fm) at different photon virtualities predicted by the light front holography 't Hooft (solid), the light front holography IMA (dashed), and the BdT longitudinal mode [59] (dot-dashed) approaches, respectively.

in Ref. [59]. We highlight that our longitudinal mode features a narrower distribution compared to others. In principle, according to Eq. (23), one would expect that the IMA and the mode in Ref. [59] are exactly same. Here, the IMA is slightly different from that due to use of a different quark mass.

### B. $\rho$-meson diffractive cross section

The exclusive vector meson production cross section depends upon the overlap of the $q\bar{q}$ component of the virtual photon wave functions with the vector meson wave functions as illustrated in Eq. (1). We present the overlap of the LFWFs after integrating over $x$ at different photon virtualities $Q^2 = 2$, 4.8 and 19.7 GeV$^2$ in Fig. 4. We compare three different overlap functions, which are different in considering the longitudinal modes in the meson wave functions: (i) the IMA that does not contain dynamical mode along the longitudinal direction, (ii) the BdT longitudinal dynamics outlined in Ref. [59], and (iii) the one containing longitudinal dynamics incorporated through the 't Hooft equation. However, we find that they lead to more or less similar behavior of the overlap functions. The peaks of the distributions undergo a shift toward lower values of $\mathbf{r}_\perp$ and decrease in magnitude as the virtuality of the photon increases.

In Fig. 5, we illustrate the three-dimensional probabilistic distributions, $|\Psi^{\Lambda}_{h,\bar{h}}(x,\mathbf{r}_\perp)|^2$, as a function of $x$ and $\mathbf{r}_\perp$ for a longitudinally (left panel) and a transversely

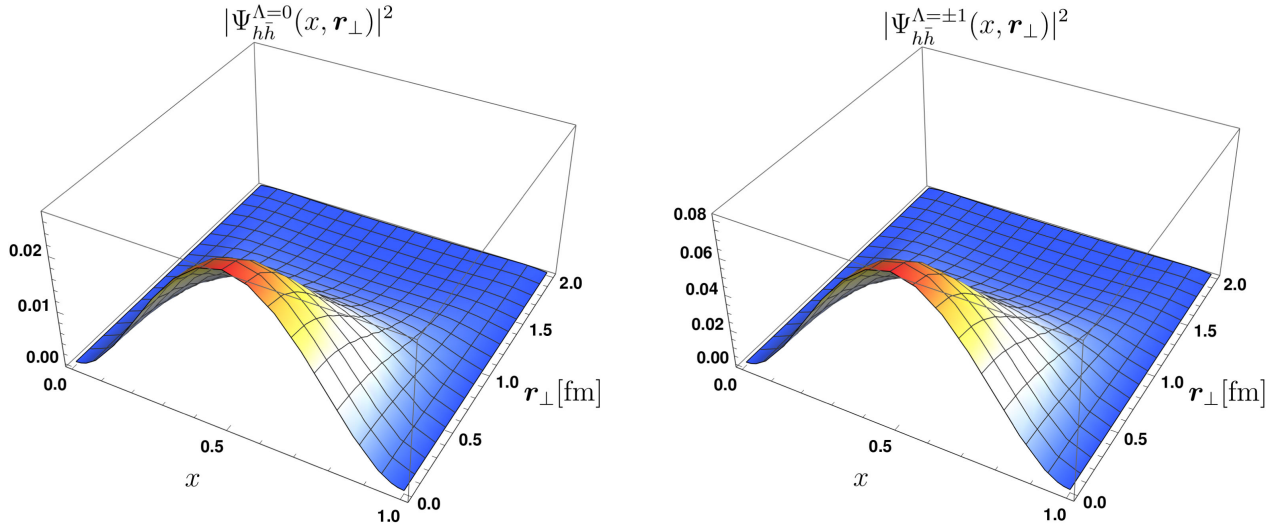


FIG. 5. Distributions of the longitudinal $|\Psi^{\Lambda=0}_{h,\bar{h}}(x,\mathbf{r}_\perp)|^2$ (left) and transverse $|\Psi^{\Lambda=\pm1}_{h,\bar{h}}(x,\mathbf{r}_\perp)|^2$ (right) LFWFs of the $\rho$-meson as functions of longitudinal momentum fraction carried by the quark $x$ and the dipole separation $\mathbf{r}_\perp$ (in fm).

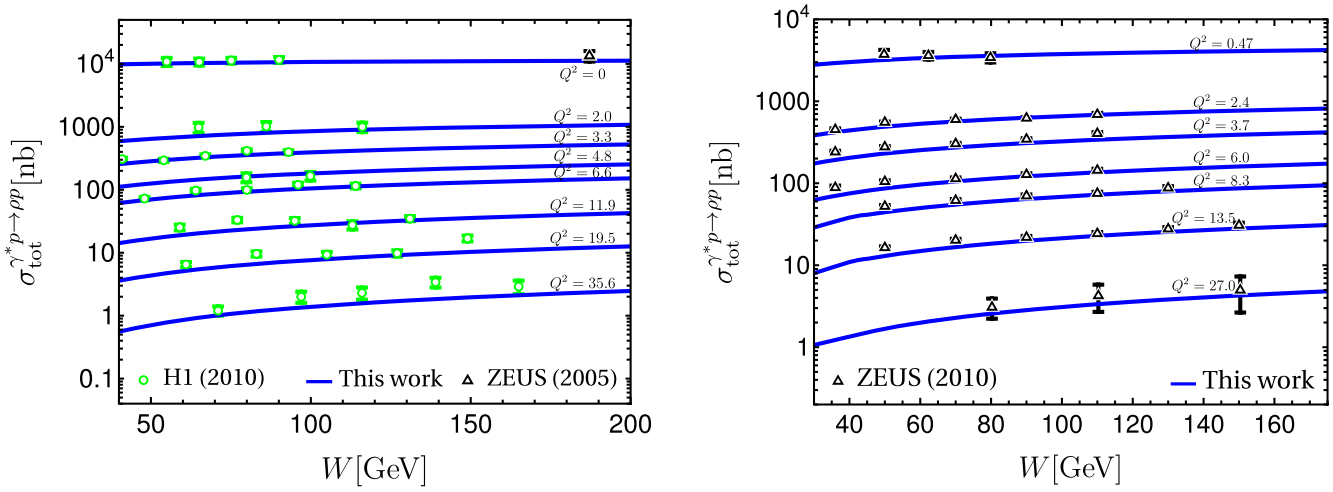


FIG. 6. Our predictions of the total diffractive cross section for $\gamma^* p \to \rho p$ as a function of $W$ (in GeV) in different $Q^2$ bins (in GeV$^2$) and compared with experimental data from H1 2010 [12,13], ZEUS 2000 data (at $Q^2 = 0$) [16] (left) and ZEUS 2010 data [12] (right).

(right panel) polarized $\rho$-meson from our resulting holographic LFWFs incorporated with longitudinal modes generated by the 't Hooft equation. We notice that the wave function peaks at $x = 0.5$ and $\mathbf{r}_\perp = 0$, and go rapidly to zero as $x \to 0$, 1 and $\mathbf{r}_\perp$ increases. Our results behaves similar to the wave functions reported in Ref. [46]. We have now all the ingredients (photon and vector meson LFWFs, and the dipole cross section) to compute the diffractive vector meson production cross section. We calculate $\rho$-meson production utilizing the CGC dipole model with parameters fitted to DIS data from HERA, as detailed in Ref. [22]. In Fig. 6, we show the total cross section as a function of $W$ for different $Q^2$ bins. On the left panel, we compare our predictions with the experimental data for $0 \leq Q^2 \leq 35.6$ GeV$^2$ from the H1 Collaboration [12,13], whereas, the right panel compares our results with the experimental data from the ZEUS Collaboration [12] in the range $0.47 \leq Q^2 \leq 27.0$ GeV$^2$. From the comparison, we observe that our predictions are in reasonable agreement with the experiments within the range of allowed uncertainty. We also note that the longitudinal dynamics implemented through the 't Hooft equation improves the predictions compared to those calculated using IMA in Ref. [22]. The differential cross section, $d\sigma/dt$, as a function of $t$ for the elastic $\rho$-meson production are shown in Fig. 7, where we compare our results with the experimental data from the H1 [12] (left panel) and ZEUS [15] (right panel) Collaboration at different values of $Q^2$. Again, we observe that our predictions show a good agreement with the measurements. However, at large $t$ and small $Q^2$, our results are somewhat underestimated for the ZEUS data.

The Figs. 8(a) and 8(b) present the longitudinal and transverse cross sections, respectively, for the diffractive $\rho$-meson production as a function of photon virtually for the fixed value of $W = 75$ GeV. We find good agreement with the experiment at HERA [12]. The total $\gamma^* p$ elastic cross section for $\rho$-meson production is also found to be in good

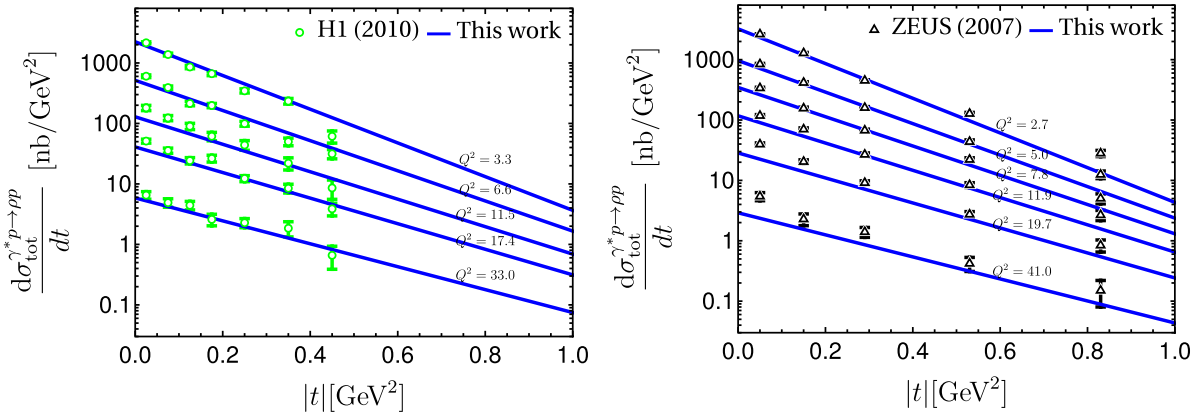


FIG. 7. Our predictions of differential cross section, $d\sigma/dt$ (in nb/GeV$^2$) for $\gamma^* p \to \rho p$ as a function of $|t|$ (in GeV$^2$) compared with H1 2010 [12] (left) and ZEUS 2007 [15] (right) data, respectively.

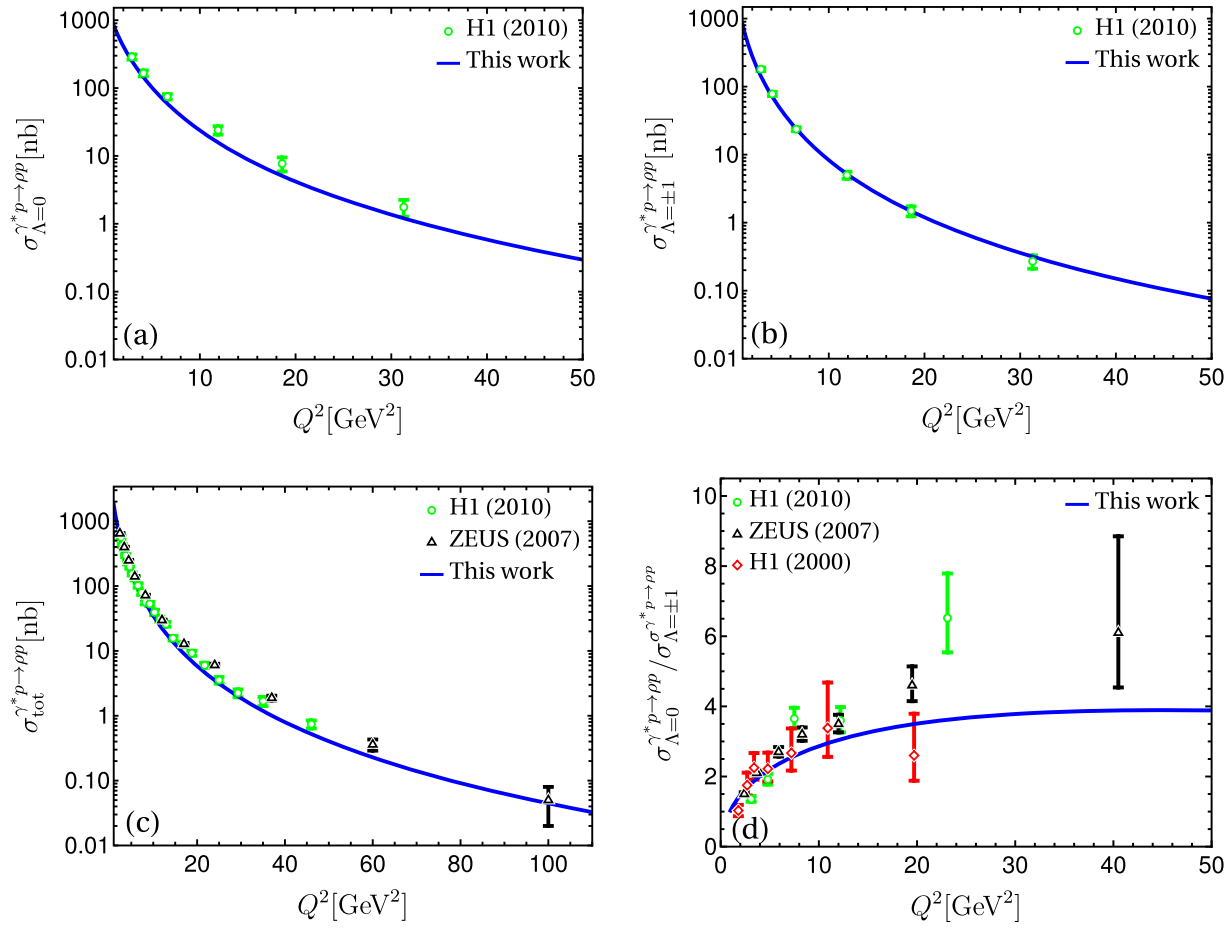


FIG. 8. Our predictions for the $Q^2$ dependence of (a) longitudinal, (b) transverse, (c) Total $\gamma^* p$ cross sections for elastic $\rho$ meson production with $W = 75$ GeV and (d) longitudinal to transverse cross section ratio compared to the H1 at $W = 75$ GeV [11,12] and ZEUS at $W = 75$ GeV [15] data.

agreement with the experiments [11,15] as can be seen in Fig. 8(c). Finally, in Fig. 8(d), we illustrate the ratio of the longitudinal to transverse cross section, $\sigma_{\Lambda=0}/\sigma_{\Lambda=\pm1}$, for $\rho$ production. We compare our prediction with the H1 2010 [12], ZEUS 2007 [15] and old 2000 H1 [11] data. Here, we notice that for the low values of $Q^2$, i.e., $Q^2 \leq 10$ GeV$^2$, our results show a good agreement with all the three datasets, whereas it slightly deviates at large $Q^2$ from the measured data.

### C. Decay constants and distribution amplitudes

In this section, we compute the decay constants and distribution amplitudes for the $\rho$-meson and compare them with the experimental data along with the theoretical predictions from other models. The vector and tensor coupling constants, $f_V$ and $f_V^T$ respectively, are defined as the local vacuum-to-hadron matrix elements [83]

$$\langle 0|\bar{q}(0)\gamma^\mu q(0)|V(P,\Lambda)\rangle = f_V M_V \epsilon_\Lambda^\mu, \tag{33}$$

and

$$\langle 0|\bar{q}(0)[\gamma^\mu,\gamma^\nu]q(0)|V(P,\Lambda)\rangle = 2f_V^T(\epsilon_\Lambda^\mu P^\nu - \epsilon_\Lambda^\nu P^\mu), \tag{34}$$

where $q(\bar{q})$ are the quark(anti-quark) field operators at same space-time points. The momentum and polarization vectors are denoted as $P^\mu$ and $\epsilon_\Lambda^\mu$, respectively. In terms of LFWFs, the decay constant can be expressed as [84]

$$f_V = \sqrt{\frac{N_c}{\pi}}\int_0^1 \mathrm{d}x\left[1+\frac{m_q^2-\nabla_{\mathbf{r}_\perp}^2}{x(1-x)M_V^2}\right]\Psi(x,\mathbf{r}_\perp)|_{\mathbf{r}_\perp=0}, \tag{35}$$

and

$$f_V^T(\mu) = \sqrt{\frac{N_c}{2\pi}}m_q\int_0^1 \mathrm{d}x\int \mathrm{d}\mathbf{r}_\perp \mu J_1(\mu\mathbf{r}_\perp)\frac{\Psi(x,\mathbf{r}_\perp)}{x(1-x)}, \tag{36}$$

where $\Psi$ is the meson LFWF given in Eq. (29) and $\mu$ is the ultraviolet cutoff scale. We note that our predictions for the tensor coupling are scale independent for $\mu^2 \geq 1$. However, it is sensitive to the quark mass $m_q$, as can be seen from Eq. (36). In the chiral limit, $m_q \to 0$, the tensor coupling vanishes, whereas the vector coupling has a nonzero value.

TABLE II. Our predictions for the electronic decay widths of the $\rho$-meson using 't Hooft equation with $m_{u,d} = 0.046$ GeV. The LF holography IMA predictions correspond to $m_{u,d} = [0.046, 0.14]$ GeV.

| $\rho$-meson | $f_V$ [MeV] | $\Gamma_{e^+e^-}$ [KeV] |
|---|---|---|
| This work | 208 | 6.294 |
| LFH (IMA) [21,22] | [210, 211] | [6.355, 6.66] |
| Exp. (PDG) [85] | 216(5) | $7.04 \pm 0.06$ |

The vector coupling can be used to calculate the electronic decay width

$$\Gamma_{V\to e^+e^-} = \frac{4\pi\alpha_{em}^2 C_V^2}{3M_V} f_V^2, \tag{37}$$

where, for the $\rho$-meson, $C_\rho = 1/\sqrt{2}$. In Table II, we present our predictions for the vector coupling constant, which is associated with the decay width of the $\rho$-meson. These predictions are compared with the results from LFhQCD with IMA approach [21,22] and experimental data [85]. Additionally, in Table III, we compare our model predictions for decay constants when $\rho$-meson is considered to be longitudinally and transversely polarized, as well as their ratio $f_\rho^\perp/f_\rho$. We compare our results with the predictions from other theoretical approaches in Table III. Our prediction for the vector coupling constant demonstrates good agreement with both the theoretical and experimental studies. However, the tensor coupling constant is significantly smaller as compared to the other predictions in the literature.

PDAs are obtainable through the vacuum-to-meson transition matrix elements of quark-antiquark nonlocal gauge-invariant operators [95–97]. The longitudinal and transverse components of the distribution amplitude for the vector meson are defined as [98]

$$f_\rho \phi_\rho^\parallel(x,\mu) = \int \mathrm{d}x^- e^{ixP^+x^-} \langle 0|\bar{q}(0)\gamma^+ q(x^-)|V(P,\Lambda=0)\rangle, \tag{38}$$

and

$$f_\rho^\perp \phi_\rho^\perp(x,\mu) = \frac{1}{2}\int \mathrm{d}x^- e^{ixP^+x^-} \langle 0|\bar{q}(0)[\epsilon^*_{\Lambda(\pm)}\cdot\gamma, \gamma^+] \times q(x^-)|V(P,\Lambda=\pm 1)\rangle. \tag{39}$$

After calculating the matrix elements, the above Eqs. (38) and (39) lead to

$$\phi_\rho^\parallel(x,\mu) = \frac{N_c}{\pi f_\rho M_\rho}\int \mathrm{d}\mathbf{r}_\perp \mu J_1(\mu \mathbf{r}_\perp)[M_V^2 x(1-x) + m_q^2 - \nabla^2_{\mathbf{r}_\perp}]\frac{\Psi(x,\mathbf{r}_\perp)}{x(1-x)}, \tag{40}$$

and

$$\phi_\rho^\perp(x,\mu) = \frac{N_c m_q}{\pi f_\rho^\perp}\int \mathrm{d}\mathbf{r}_\perp \mu J_1(\mu \mathbf{r}_\perp)\frac{\Psi(x,\mathbf{r}_\perp)}{x(1-x)}, \tag{41}$$

where $f_\rho$ and $f_\rho^\perp$ are the vector and tensor couplings, which are given in Eq. (35) and (36), respectively. The longitudinal ($\phi_\rho^\parallel$) and transverse ($\phi_\rho^\perp$) components of the PDAs can be normalized as [99]

$$\int_0^1 \mathrm{d}x \phi_\rho^\parallel(x,\mu) = 1, \quad \text{and} \quad \int_0^1 \mathrm{d}x \phi_\rho^\perp(x,\mu) = 1. \tag{42}$$

Figure 9 illustrates the normalized longitudinal and transverse components of $\rho$-meson PDAs and their comparison with hLFQCD associated with IMA predictions at nonzero light quark mass, $m_q \simeq 0.046$ GeV, as well as with the dynamical longitudinal mode reported in Ref. [59]. We find

TABLE III. Using the value of light quark masses, $m_{u,d} = 0.046$ GeV, we predict the longitudinal and transverse decay constants for the $\rho$-meson, as well as the ratio between them and compared with other model estimate. Our predictions are at a scale of $\mu = 1$ GeV.

| Reference | Approach | $f_\rho$ [MeV] | $f_\rho^\perp$ [MeV] | $f_\rho^\perp/f_\rho$ |
|---|---|---|---|---|
| This work | LFH ('t Hooft) | 208 | 36 | 0.17 |
| Ref. [22,86] | LFH (IMA) | [211, 214] | [95, 36] | [0.45, 0.17] |
| Ref. [87] | LFQM | $208 \pm 7$ | $152 \pm 9$ | |
| Ref. [88] | Sum Rules | $198 \pm 7$ | $152 \pm 9$ | |
| Ref. [89] | Sum Rules | $206 \pm 7$ | $145 \pm 9$ | $0.70 \pm 0.04$ |
| Ref. [90] | Lattice (continuum) | | | $0.72 \pm 0.02$ |
| Ref. [91] | Lattice (finite) | | | $0.742 \pm 0.014$ |
| Ref. [92] | Lattice (unquenched) | | $159 \pm 0.008$ | $0.76 \pm 0.04$ |
| Ref. [93] | Dyson-Schwinger | 212 | 156 | 0.73 |
| Ref. [94] | LFQM: Linear [HO] | 246[215] | 187[163] | 0.76[0.80] |

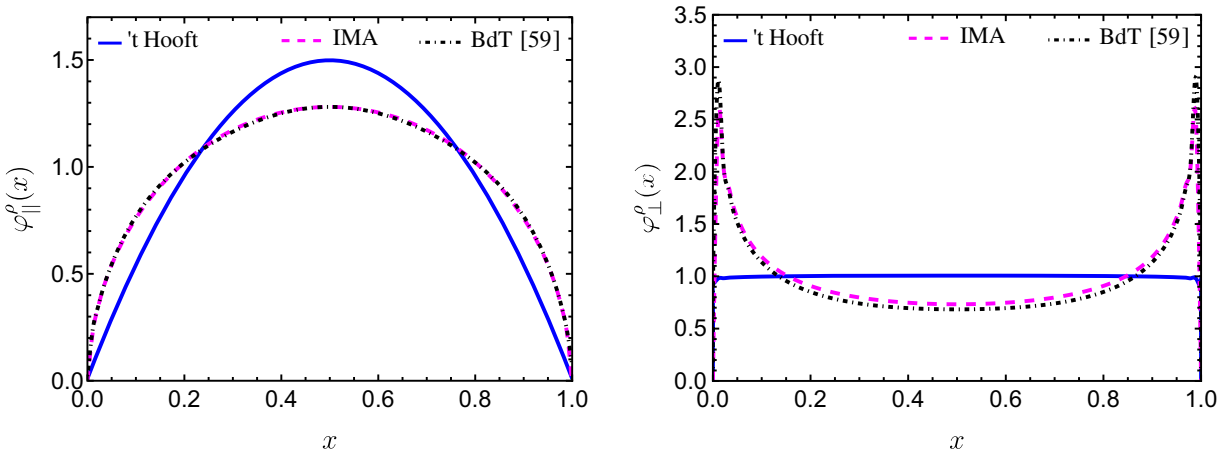


FIG. 9. Our results for the PDAs for longitudinally (left) and transversely (right) polarized $\rho$-mesons (in solid blue). We compared them with IMA PDAs (magenta-dashed) and BdT PDAs [59] (black-dot dashed).

that our $\phi^{\parallel}_{\rho}(x)$ exhibits narrower distribution, while $\phi^{\perp}_{\rho}(x)$ shows flat distribution compared to those evaluated using hLFQCD associated with IMA and the longitudinal mode in Ref. [59].

We calculate the moments of the PDAs, also known as $\xi$-moments, in order to quantitatively compare with other approaches. The $n$th moment is defined as [99],

$$\langle \xi^n \rangle = \langle (2x-1)^n \rangle = \int_0^1 \mathrm{d}x (2x-1)^n \phi(x). \quad (43)$$

In Table IV, we compare our model results for the computed $\xi$-moments at $\mu \sim 1$ GeV with other theoretical estimations for $n = 2, 4, 6, 8$, and 10. For the odd values of $n$, the moments vanish due to the isospin symmetry. Our $\xi$-moments are more or less consistent with other theoretical studies.

### D. $\rho$-meson form factors

The LFWFs also provide direct access to electromagnetic form factors. The Lorentz-invariant electromagnetic

TABLE IV. Computed moments of the $\rho$-meson PDAs, Eq. (43), compared with selected results obtained elsewhere, using: AdS/QCD models for LFWFs fitted to HERA data [100]; QCD sum rules [98,101]; nonlocal condensates [102,103]; light-front quark model [94]; light-front holographic QCD [22], and lattice-QCD [104,105].

| $\langle (2x-1)^m \rangle$ | | $m=2$ | 4 | 6 | 8 | 10 |
|---|---|---|---|---|---|---|
| This work | $\parallel$ | 0.20 | 0.087 | 0.048 | 0.031 | 0.022 |
| | $\perp$ | 0.25 | 0.13 | 0.079 | 0.055 | 0.042 |
| $\varphi = \varphi^{\mathrm{asy}}$ | | 0.20 | 0.086 | 0.048 | 0.030 | 0.021 |
| $\varphi =$ constant | | 0.33 | 0.2 | 0.14 | 0.11 | 0.091 |
| [22] | $\parallel$ | 0.25 | 0.12 | 0.075 | 0.052 | 0.038 |
| | $\perp$ | 0.26 | 0.13 | 0.079 | 0.054 | 0.039 |
| [106] | $\parallel$ | 0.22 | 0.103 | 0.066 | 0.046 | 0.035 |
| [100] | $\parallel$ | 0.23 | 0.11 | 0.062 | 0.041 | 0.029 |
| | $\perp$ | 0.26 | 0.13 | 0.079 | 0.054 | 0.039 |
| [101] | $\parallel$ | 0.26 | | | | |
| | $\perp$ | 0.27 | | | | |
| [102] | $\parallel$ | 0.23(1) | 0.095(5) | 0.051(4) | 0.030(2) | 0.020(5) |
| | $\perp$ | 0.33(1) | | | | |
| [103] | $\parallel$ | 0.22(2) | 0.089(9) | 0.048(5) | 0.030(3) | 0.022(2) |
| | $\perp$ | 0.11(1) | 0.022(2) | | | |
| [94] | $\parallel$ | 0.20(1) | 0.085(5) | 0.045(5) | | |
| | $\perp$ | 0.21(1) | 0.095(5) | 0.05(1) | | |
| [104,105] | | 0.25(2)(2) | | | | |

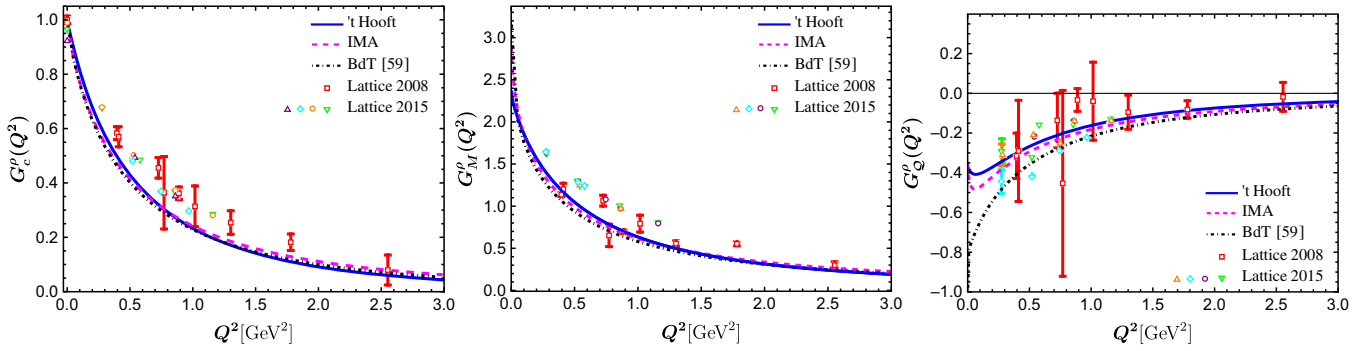


FIG. 10. Left: the charge ($G_C^\rho$); middle: the magnetic ($G_M^\rho$); and right: the quadrupole ($G_Q^\rho$) form factors for the $\rho$-meson as a functions of $Q^2$. Our results are compared with Lattice QCD predictions [115,116].

Form factors $F_i$ ($i = 1, 2, 3$) for a vector meson (spin-1) can be obtained by calculating the matrix elements of the electromagnetic current $J^\mu$ as [107,108],

$$\begin{aligned}\langle V(P',\Lambda')|J^\mu|V(P,\Lambda)\rangle &= -\epsilon^*_{\Lambda'}\cdot\epsilon_\Lambda(P+P')^\mu F_1(Q^2)\\ &+(\epsilon^\mu_\Lambda q\cdot\epsilon^*_{\Lambda'}-\epsilon^{*\mu}_{\Lambda'}q\cdot\epsilon_\Lambda)F_2(Q^2)\\ &+\frac{(\epsilon^*_{\Lambda'}\cdot q)(\epsilon_\Lambda\cdot q)}{2M_V^2}\\ &\times(P+P')^\mu F_3(Q^2) \qquad (44)\end{aligned}$$

where $\epsilon_\Lambda$ and $\epsilon_{\Lambda'}$ are the polarization vectors of the initial and final mesons, respectively. We employ the Breit frame, where the momentum transfer occurs only in one transverse direction, i.e., $(q^+ = 0, q_x = Q, q_y = 0)$, and $P_\perp = -P'_\perp$ [109,110]. The momenta of the initial and final states are defined as: $P^\mu = (M_V\sqrt{1+\eta}, M_V\sqrt{1+\eta}, -Q/2, 0)$ and $P'^\mu = (M_V\sqrt{1+\eta}, M_V\sqrt{1+\eta}, Q/2, 0)$, respectively with $\eta = Q^2/4M_V^2$. We follow the notation $p^\mu = (p^+, p^-, p^1, p^2)$. We compute the form factors by considering the plus component of the electromagnetic current, $J^+(0)$. The matrix elements of $J^+(0)$ can be expressed as [111,112]

$$\begin{aligned}I^+_{\Lambda',\Lambda}(Q^2) &\triangleq \langle V(P',\Lambda')\left|\frac{J^+(0)}{2P^+}\right|V(P,\Lambda)\rangle\\ &=\sum_{h,\bar h}\int_0^1\int_0^\infty\frac{dx d^2\mathbf{k}_\perp}{16\pi^3}\Psi^{\Lambda'*}_{h\bar h}(x,\mathbf{k}_\perp+(1-x)\mathbf{q}_\perp)\\ &\times\Psi^{\Lambda}_{h\bar h}(x,\mathbf{k}_\perp), \qquad (45)\end{aligned}$$

where $\Lambda$ and $\Lambda'$ denote the helicities of the incoming and outgoing vector mesons, respectively. There are a total of nine matrix elements of the electromagnetic current, $I^+_{\Lambda\Lambda'}$ for $\Lambda, \Lambda' = 0, \pm 1$. Using the light-front parity and time reversal invariance, one can reduce it to only four matrix elements: $I^+_{1,1}, I^+_{1,-1}, I^+_{1,0}$, and $I^+_{0,0}$. Note that the physical charge ($G_C$), magnetic ($G_M$), and quadrupole ($G_Q$) form factors are often employed to describe the electromagnetic properties of a hadron, instead of the Lorentz invariant electromagnetic form factors, $F_i$. However, these two types of form factors are related to each other such that

$$\begin{aligned}&G_C = F_1+\frac{2}{3}\eta G_Q, \qquad G_M = -F_2,\\ &G_Q = F_1+F_2+(1+\eta)F_3.\end{aligned}$$

We obtain the static charge ($e$), magnetic moment ($\mu$) and quadrupole moment ($\mathcal{Q}$) of the hadron from the above form factors at zero momentum transfer,

$$eG_{\rm C}(0) = e, \qquad eG_{\rm M}(0) = 2M_V\mu, \qquad -eG_{\rm Q} = M_V^2\mathcal{Q}.$$

Notably, there are different prescriptions, for example, Grach and Kondratyuk (GK) [113], and Brodsky and Hiller (BH) [114], to calculate such type of form factors. Nevertheless, we compute these physical form factors following the BH prescription, which includes the zero-mode contributions. In the BH prescription, the form factors are defined as,

$$\begin{aligned}G^{\rm BH}_{\rm C}(Q^2) &= \frac{1}{2P^+(1+2\eta)}\left[\frac{3-2\eta}{3}I^+_{0,0}+\frac{16}{3}\eta\frac{I^+_{1,0}}{\sqrt{2\eta}}\right.\\ &\left.+\frac{2}{3}(2\eta-1)I^+_{1,-1}\right],\\ G^{\rm BH}_{\rm M}(Q^2) &= \frac{2}{2P^+(1+2\eta)}\left[I^+_{0,0}+\frac{(2\eta-1)}{\sqrt{2\eta}}I^+_{1,0}-I^+_{1,-1}\right],\\ G^{\rm BH}_{\rm Q}(Q^2) &= -\frac{1}{2P^+(1+2\eta)}\left[I^+_{0,0}-2\frac{I^+_{1,0}}{\sqrt{2\eta}}+\frac{1+\eta}{\eta}I^+_{1,-1}\right].\end{aligned} \qquad (46)$$

We show the variation of the charge, magnetic, and quadrupole elastic form factors with $Q^2$ in Fig. 10, where we include the results generated using the IMA and the longitudinal mode in Ref. [59], and Lattice QCD [115,116] for comparison. We observe a good agreement of our results with the latice QCD simulations. From the charge form factor, we further calculate the charge root-mean-squared (rms) radius of the $\rho$ meson, which is defined as [117],

TABLE V. Comparison of the $\rho$-meson charge radii $\sqrt{\langle r_\rho^2\rangle}$ (in fm), magnetic moments $\mu_\rho$ (in units of Bohr magneton) and quadrupole moments $\mathcal{Q}_\rho$ (in fm$^2$) with various theoretical approaches.

| | This work | | | BLFQ | BSE | Lattice QCD | Lattice QCD | LFQM | NJL model |
|---|---|---|---|---|---|---|---|---|---|
| | 't Hooft | IMA | BdT | [111] | [118] | [119] | [121] | [108] | [120] |
| $\sqrt{\langle r_\rho^2\rangle}$ | 0.75 | 0.94 | 0.91 | 0.44 | 0.73 | 0.819(42) | 0.55(5) | 0.52 | 0.82 |
| $\mu_\rho$ | 2.40 | 2.90 | 3.30 | 2.15 | 2.01 | 2.067(76) | 2.17(10) | 1.92 | 2.48 |
| $\mathcal{Q}_\rho$ | −0.027 | −0.023 | −0.066 | −0.063 | −0.026 | −0.0452(61) | −0.035 | −0.028 | −0.070 |

$$\langle r_\rho^2\rangle = -\frac{6}{G_C(0)}\lim_{Q^2\to 0}\frac{\partial G_C(Q^2)}{\partial Q^2}. \tag{47}$$

We present our results for the static properties of the $\rho$ meson: rms charge radius, magnetic moment, and quadrupole moment in Table V, where we compare them with the predictions from various theoretical approaches. We observe that our result for the charge radius is close to the results from BSE [118], lattice QCD [119], and NJL model [120]. On the other hand, our magnetic moment is more or less consistent with all other studies summarized in Table V. The quadrupole moment agrees well with the results from BSE [118], LFQM [108], and lattice QCD [121], and they differ from other predictions.

## V. CONCLUSION

The 't Hooft equation is complementary to the light-front holographic Schrödinger equation, in governing the longitudinal dynamics of quark-antiquark mesons. We have shown that together, they predict remarkably well the mass spectroscopy of $\rho$-meson family without further adjusting parameters: the universal transverse confinement scale $\kappa = 0.523$ GeV, the longitudinal confinement scale $g = 0.109$ GeV, and the light quark mass $m_q = 0.046$ GeV, which were determined to predict the pion spectroscopy and its structure [69]. In conjunction with the CGC dipole cross section, the $\rho$-meson holographic LFWFs after incorporating the longitudinal mode generated by the 't Hooft equation lead to a good description of the cross-section data for the diffractive $\rho$-meson electroproduction at different energies. Using the resulting LFWFs, we have calculated the decay constant, distribution amplitude, electromagnetic form factors, charge radius, magnetic moment, and quadrupole moment of the $\rho$-meson. Interestingly, we have noticed that although, the electromagnetic form factors in our approach agree well with the LFH-IMA predictions, they differ from each other in describing the distribution amplitudes. We have found that the vector coupling is close to the experimentally measured data and various theoretical predictions; however, the tensor coupling constant is significantly smaller compared to the other predictions in the literature. Meanwhile, the moments of distribution amplitudes and the static properties: charge radius, magnetic moment, and quadrupole moment have been found to be consistent with other theoretical as well as lattice QCD results.

## ACKNOWLEDGMENTS

We thank Ruben Sandapen and Mohammad Ahmady for fruitful discussions. C. M. is supported by new faculty start up funding by the Institute of Modern Physics, Chinese Academy of Sciences, Grant No. E129952YR0. C. M. also thanks the Chinese Academy of Sciences Presidents International Fellowship Initiative for the support via Grant No. 2021PM0023. S. K. is supported by Research Fund for International Young Scientists, Grant No. 12250410251, from the National Natural Science Foundation of China (NSFC), and China Postdoctoral Science Foundation (CPSF), Grant No. E339951SR0.

[1] L. V. Gribov, E. M. Levin, and M. G. Ryskin, Semihard processes in QCD, Phys. Rep. **100**, 1 (1983).
[2] N. N. Nikolaev and B. G. Zakharov, Colour transparency and scaling properties of nuclear shadowing in deep inelastic scattering, Z. Phys. C **49**, 607 (1991).
[3] A. Mueller and B. Patel, Single and double BFKL pomeron exchange and a dipole picture of high energy hard processes, Nucl. Phys. **B425**, 471 (1994).
[4] J. Jalilian-Marian and Y. V. Kovchegov, Saturation physics and deuteron–gold collisions at RHIC, Prog. Part. Nucl. Phys. **56**, 104 (2006).
[5] L. D. McLerran, The color glass condensate and small x physics: Four lectures, Lect. Notes Phys. **583**, 291 (2002).
[6] E. Iancu, A. Leonidov, and L. McLerran, The Color Glass Condensate: An Introduction (2002), pp. 73–145, arXiv: hep-ph/0202270.

[7] A. H. Mueller, Soft gluons in the infinite momentum wave function and the BFKL Pomeron, Nucl. Phys. **B415**, 373 (1994).
[8] J. Nemchik, N. N. Nikolaev, E. Predazzi, and B. G. Zakharov, Color dipole phenomenology of diffractive electroproduction of light vector mesons at HERA, Z. Phys. C **75**, 71 (1997).
[9] J. Nemchik, N. Nikolaev, E. Predazzi, and B. Zakharov, Color dipole systematics of diffractive photo- and electroproduction of vector mesons, Phys. Lett. B **374**, 199 (1996).
[10] J. Nemchik, N. Nikolaev, and B. Zakharov, Scanning the BFKL Pomeron in elastic production of vector mesons at hera, Phys. Lett. B **341**, 228 (1994).
[11] C. Adloff *et al.* (H1 Collaboration), Elastic electroproduction of rho mesons at HERA, Eur. Phys. J. C **13**, 371 (2000).
[12] F. D. Aaron *et al.* (H1 Collaboration), Diffractive electroproduction of rho and phi mesons at HERA, J. High Energy Phys. 05 (2010) 032.
[13] S. Aid *et al.* (H1 Collaboration), Elastic photoproduction of $\rho^0$ mesons at HERA, Nucl. Phys. **B463**, 3 (1996).
[14] S. Chekanov *et al.* (ZEUS Collaboration), Exclusive electroproduction of $\phi$ mesons at HERA, Nucl. Phys. **B718**, 3 (2005).
[15] S. Chekanov *et al.* (ZEUS Collaboration), Exclusive rho0 production in deep inelastic scattering at HERA, PMC Phys. A **1**, 6 (2007).
[16] J. Breitweg *et al.* (ZEUS Collaboration), Elastic and proton dissociative $\rho^0$ photoproduction at HERA, Eur. Phys. J. C **2**, 247 (1998).
[17] S. J. Brodsky, G. F. de Téramond, H. G. Dosch, and J. Erlich, Light-front holographic QCD and emerging confinement, Phys. Rep. **584**, 1 (2015).
[18] G. 't Hooft, A two-dimensional model for mesons, Nucl. Phys. **B75**, 461 (1974).
[19] S. J. Brodsky, G. F. de Teramond, H. G. Dosch, and J. Erlich, Light-front holographic QCD and emerging confinement, Phys. Rep. **584**, 1 (2015).
[20] S. J. Brodsky and G. F. de Teramond, AdS/CFT and light-front QCD, Subnucl. Ser. **45**, 139 (2009).
[21] J. R. Forshaw and R. Sandapen, AdS/QCD holographic wave function for the $\rho$ meson and diffractive $\rho$ meson electroproduction, Phys. Rev. Lett. **109**, 081601 (2012).
[22] M. Ahmady, R. Sandapen, and N. Sharma, Diffractive $\rho$ and $\phi$ production at HERA using a holographic AdS/QCD light-front meson wave function, Phys. Rev. D **94**, 074018 (2016).
[23] G. Watt and H. Kowalski, Impact parameter dependent color glass condensate dipole model, Phys. Rev. D **78**, 014016 (2008).
[24] H. Kowalski, L. Motyka, and G. Watt, Exclusive diffractive processes at HERA within the dipole picture, Phys. Rev. D **74**, 074016 (2006).
[25] J. R. Forshaw and G. Shaw, Gluon saturation in the colour dipole model?, J. High Energy Phys. 12 (2005) 052.
[26] S. Chekanov *et al.* (ZEUS Collaboration), Measurement of the neutral current cross-section and F(2) structure function for deep inelastic e + p scattering at HERA, Eur. Phys. J. C **21**, 443 (2001).
[27] C. Adloff *et al.* (H1 Collaboration), Deep inelastic inclusive e p scattering at low x and a determination of alpha (s)., Eur. Phys. J. C **21**, 33 (2001).
[28] F. D. Aaron *et al.* (H1, ZEUS Collaborations), Combined measurement and QCD analysis of the inclusive e+- p scattering cross sections at HERA, J. High Energy Phys. 01 (2000) 109.
[29] C. Contreras, E. Levin, and I. Potashnikova, CGC/saturation approach: A new impact-parameter dependent model, Nucl. Phys. **A948**, 1 (2016).
[30] E. Iancu, K. Itakura, and S. Munier, Saturation and BFKL dynamics in the hera data at small-x, Phys. Lett. B **590**, 199 (2004).
[31] G. P. Lepage and S. J. Brodsky, Exclusive processes in perturbative quantum chromodynamics, Phys. Rev. D **22**, 2157 (1980).
[32] H. G. Dosch, T. Gousset, G. Kulzinger, and H. J. Pirner, Vector meson leptoproduction and nonperturbative gluon fluctuations in QCD, Phys. Rev. D **55**, 2602 (1997).
[33] G. F. de Téramond and S. J. Brodsky, Light-front holography: A first approximation to QCD, Phys. Rev. Lett. **102**, 081601 (2009).
[34] A. H. Rezaeian and I. Schmidt, Impact-parameter dependent color glass condensate dipole model and new combined HERA data, Phys. Rev. D **88**, 074016 (2013).
[35] I. Balitsky, Operator expansion for high-energy scattering, Nucl. Phys. **B463**, 99 (1996).
[36] Y. V. Kovchegov, Small-x $F_2$ structure function of a nucleus including multiple Pomeron exchanges, Phys. Rev. D **60**, 034008 (1999).
[37] Y. V. Kovchegov, Unitarization of the BFKL pomeron on a nucleus, Phys. Rev. D **61**, 074018 (2000).
[38] J. Jalilian-Marian, A. Kovner, A. Leonidov, and H. Weigert, The BFKL equation from the Wilson renormalization group, Nucl. Phys. **B504**, 415 (1997).
[39] J. Jalilian-Marian, A. Kovner, A. Leonidov, and H. Weigert, Wilson renormalization group for low x physics: Towards the high density regime, Phys. Rev. D **59**, 014014 (1998).
[40] E. Iancu, A. Leonidov, and L. D. McLerran, Nonlinear gluon evolution in the color glass condensate. 1., Nucl. Phys. **A692**, 583 (2001).
[41] E. Iancu, A. Leonidov, and L. D. McLerran, The renormalization group equation for the color glass condensate, Phys. Lett. B **510**, 133 (2001).
[42] H. Weigert, Unitarity at small Bjorken x, Nucl. Phys. **A703**, 823 (2002).
[43] A. H. Rezaeian, M. Siddikov, M. Van de Klundert, and R. Venugopalan, Analysis of combined HERA data in the impact-parameter dependent saturation model, Phys. Rev. D **87**, 034002 (2013).
[44] H. Abramowicz *et al.* (H1, ZEUS Collaborations), Combination of measurements of inclusive deep inelastic $e^{\pm}p$ scattering cross sections and QCD analysis of HERA data, Eur. Phys. J. C **75**, 580 (2015).
[45] G. Kulzinger, H. G. Dosch, and H. J. Pirner, Diffractive photoproduction and leptoproduction of vector mesons rho, rho-prime and rho-prime-prime, Eur. Phys. J. C **7**, 73 (1999).

[46] J. R. Forshaw, R. Sandapen, and G. Shaw, Color dipoles and $\rho, \varphi$ electroproduction, Phys. Rev. D **69**, 094013 (2004).

[47] Y. Oh, H. Kim, and S. H. Lee, $\Theta^+$ baryon production in KN and NN reactions, Phys. Rev. D **69**, 074016 (2004).

[48] S. Kaur, C. Mondal, and H. Dahiya, Light-front holographic $\rho$-meson distributions in the momentum space, J. High Energy Phys. 01 (2021) 136.

[49] M. Ahmady, S. Kaur, C. Mondal, and R. Sandapen, Light-front holographic radiative transition form factors for light mesons, Phys. Rev. D **102**, 034021 (2020).

[50] G. F. de Téramond and S. J. Brodsky, Hadronic spectrum of a holographic dual of QCD, Phys. Rev. Lett. **94**, 201601 (2005).

[51] S. J. Brodsky and G. F. de Téramond, Hadronic spectra and light-front wave functions in holographic QCD, Phys. Rev. Lett. **96**, 201601 (2006).

[52] S. J. Brodsky and G. F. de Teramond, Hadronic spectra and light-front wavefunctions in holographic QCD, Phys. Rev. Lett. **96**, 201601 (2006).

[53] G. F. de Teramond and S. J. Brodsky, Hadronic spectrum of a holographic dual of QCD, Phys. Rev. Lett. **94**, 201601 (2005).

[54] G. F. de Teramond and S. J. Brodsky, Light-front holography: A first approximation to QCD, Phys. Rev. Lett. **102**, 081601 (2009).

[55] S. J. Brodsky, G. F. De Téramond, and H. G. Dosch, Threefold complementary approach to holographic QCD, Phys. Lett. B **729**, 3 (2014).

[56] S. J. Brodsky and G. F. de Teramond, Light-front dynamics and AdS/QCD correspondence: The pion form factor in the space- and time-like regions, Phys. Rev. D **77**, 056007 (2008).

[57] S. J. Brodsky and G. F. de Teramond, Light-front dynamics and AdS/QCD correspondence: Gravitational form factors of composite hadrons, Phys. Rev. D **78**, 025032 (2008).

[58] Y. Li and J. P. Vary, Light-front holography with chiral symmetry breaking, Phys. Lett. B **825**, 136860 (2022).

[59] G. F. de Teramond and S. J. Brodsky, Longitudinal dynamics and chiral symmetry breaking in holographic light-front QCD, Phys. Rev. D **104**, 116009 (2021).

[60] R. Swarnkar and D. Chakrabarti, Meson structure in light-front holographic QCD, Phys. Rev. D **92**, 074023 (2015).

[61] M. Ahmady, S. Kaur, C. Mondal, and R. Sandapen, Light-front holographic radiative transition form factors for light mesons, Phys. Rev. D **102**, 034021 (2020).

[62] M. Ahmady, S. Keller, M. Thibodeau, and R. Sandapen, Reexamination of the rare decay $B_s \to \phi\mu^+\mu^-$ using holographic light-front QCD, Phys. Rev. D **100**, 113005 (2019).

[63] M. Ahmady, C. Mondal, and R. Sandapen, Predicting the light-front holographic TMDs of the pion, Phys. Rev. D **100**, 054005 (2019).

[64] M. Ahmady, C. Mondal, and R. Sandapen, Dynamical spin effects in the holographic light-front wavefunctions of light pseudoscalar mesons, Phys. Rev. D **98**, 034010 (2018).

[65] M. Ahmady, F. Chishtie, and R. Sandapen, Spin effects in the pion holographic light-front wavefunction, Phys. Rev. D **95**, 074008 (2017).

[66] Y. Li, P. Maris, X. Zhao, and J. P. Vary, Heavy quarkonium in a holographic basis, Phys. Lett. B **758**, 118 (2016).

[67] M. Ahmady, H. Dahiya, S. Kaur, C. Mondal, R. Sandapen, and N. Sharma, Extending light-front holographic QCD using the 't Hooft equation, Phys. Lett. B **823**, 136754 (2021).

[68] M. Ahmady, S. Kaur, S. L. MacKay, C. Mondal, and R. Sandapen, Hadron spectroscopy using the light-front holographic Schrödinger equation and the 't Hooft equation, Phys. Rev. D **104**, 074013 (2021).

[69] M. Ahmady, S. Kaur, C. Mondal, and R. Sandapen, Pion spectroscopy and dynamics using the holographic light-front Schrödinger equation and the 't Hooft equation, Phys. Lett. B **836**, 137628 (2023).

[70] S. S. Chabysheva and J. R. Hiller, Dynamical model for longitudinal wave functions in light-front holographic QCD, Ann. Phys. (Amsterdam) **337**, 143 (2013).

[71] V. E. Lyubovitskij and I. Schmidt, Meson masses and decay constants in holographic QCD consistent with ChPT and HQET, Phys. Rev. D **105**, 074009 (2022).

[72] C. M. Weller and G. A. Miller, Confinement in two-dimensional QCD and the infinitely long pion, Phys. Rev. D **105**, 036009 (2022).

[73] M. Rinaldi, F. A. Ceccopieri, and V. Vento, The pion in the graviton soft-wall model: Phenomenological applications, Eur. Phys. J. C **82**, 626 (2022).

[74] N. Sharma, Exclusive diffractive $J/\psi$ and $\psi(2S)$ production in dipole model using a holographic AdS/QCD light-front wavefunction with longitudinal confinement, Phys. Rev. D **109**, 014019 (2024).

[75] E. Katz and T. Okui, The 't Hooft model as a hologram, J. High Energy Phys. 01 (2009) 013.

[76] A. R. Zhitnitsky, On chiral symmetry breaking in QCD in two-dimensions ($N_c \to$ infinity)., Phys. Lett. B **165**, 405 (1985).

[77] B. Grinstein and R. F. Lebed, Explicit quark-hadron duality in heavy-light meson weak decays in the 't Hooft model, Phys. Rev. D **57**, 1366 (1998).

[78] B. Grinstein and P. F. Mende, Heavy mesons in two dimensions, Phys. Rev. Lett. **69**, 1018 (1992).

[79] X. Ji, Y. Liu, and I. Zahed, Mass structure of hadrons and light-front sum rules in the 't Hooft model, Phys. Rev. D **103**, 074002 (2021).

[80] R. F. Lebed and N. G. Uraltsev, Precision studies of duality in the 't Hooft model, Phys. Rev. D **62**, 094011 (2000).

[81] B. Ma and C.-R. Ji, Interpolating 't Hooft model between instant and front forms, Phys. Rev. D **104**, 036004 (2021).

[82] M. Ahmady, S. L. MacKay, S. Kaur, C. Mondal, and R. Sandapen, Hadron spectroscopy using the light-front holographic Schrödinger equation and the 't Hooft equation, Phys. Rev. D **104**, 074013 (2021).

[83] H.-M. Choi and C.-R. Ji, Consistency of the light-front quark model with chiral symmetry in the pseudoscalar meson analysis, Phys. Rev. D **91**, 014018 (2015).

[84] M. Ahmady and R. Sandapen, Predicting $\bar{b}^\circ \to \rho^\circ\gamma$ and $\bar{b}_s^\circ \to \rho^\circ\gamma$ using holographic AdS/QCD distribution amplitudes for the $\rho$ meson, Phys. Rev. D **87**, 054013 (2013).

[85] K. A. Olive *et al.* (Particle Data Group), Review of particle physics, Chin. Phys. C **38**, 090001 (2014).

[86] M. R. Ahmady, R. Campbell, S. Lord, and R. Sandapen, Predicting the $b \to \rho$ form factors using AdS/QCD distribution amplitudes for the $\rho$ meson, Phys. Rev. D **88**, 074031 (2013).
[87] H.-M. Choi, C.-R. Ji, Z. Li, and H.-Y. Ryu, Variational analysis of mass spectra and decay constants for ground state pseudoscalar and vector mesons in the light-front quark model, Phys. Rev. C **92**, 055203 (2015).
[88] P. Ball and V. M. Braun, Exclusive semileptonic and rare $b$ meson decays in QCD, Phys. Rev. D **58**, 094016 (1998).
[89] P. Ball, V. M. Braun, and A. Lenz, Twist-4 distribution amplitudes of the K* and phi mesons in QCD, J. High Energy Phys. 08 (2007) 090.
[90] D. Becirevic, V. Lubicz, F. Mescia, and C. Tarantino, Coupling of the light vector meson to the vector and to the tensor current, J. High Energy Phys. 05 (2003) 007.
[91] V. M. Braun, T. Burch, C. Gattringer, M. Göckeler, G. Lacagnina, S. Schaefer, and A. Schäfer (Bern-Graz-Regensburg Collaboration), Lattice calculation of vector meson couplings to the vector and tensor currents using chirally improved fermions, Phys. Rev. D **68**, 054501 (2003).
[92] K. Jansen, C. McNeile, C. Michael, and C. Urbach, Meson masses and decay constants from unquenched lattice QCD, Phys. Rev. D **80**, 054510 (2009).
[93] F. Gao, L. Chang, Y.-X. Liu, C. D. Roberts, and S. M. Schmidt, Parton distribution amplitudes of light vector mesons, Phys. Rev. D **90**, 014011 (2014).
[94] H.-M. Choi and C.-R. Ji, Distribution amplitudes and decay constants for $(\pi, k, \rho, K^*)$ mesons in the light-front quark model, Phys. Rev. D **75**, 034019 (2007).
[95] G. P. Lepage and S. J. Brodsky, Exclusive processes in perturbative quantum chromodynamics, Phys. Rev. D **22**, 2157 (1980).
[96] V. L. Chernyak and A. R. Zhitnitsky, Asymptotic behavior of exclusive processes in QCD, Phys. Rep. **112**, 173 (1984).
[97] S. J. Brodsky and G. P. Lepage, Exclusive processes in quantum chromodynamics, Adv. Ser. Dir. High Energy Phys. **5**, 93 (1989).
[98] P. Ball and V. M. Braun, $\rho$ meson light-cone distribution amplitudes of leading twist reexamined, Phys. Rev. D **54**, 2182 (1996).
[99] H.-M. Choi and C.-R. Ji, Distribution amplitudes and decay constants for (pi, K, rho, K*) mesons in light-front quark model, Phys. Rev. D **75**, 034019 (2007).
[100] J. R. Forshaw and R. Sandapen, Extracting the rho meson wavefunction from HERA data, J. High Energy Phys. 11 (2010) 037.
[101] P. Ball, V. M. Braun, Y. Koike, and K. Tanaka, Higher twist distribution amplitudes of vector mesons in QCD: Formalism and twist—three distributions, Nucl. Phys. **B529**, 323 (1998).
[102] A. P. Bakulev and S. V. Mikhailov, The rho meson and related meson wave functions in QCD sum rules with nonlocal condensates, Phys. Lett. B **436**, 351 (1998).
[103] A. V. Pimikov, S. V. Mikhailov, and N. G. Stefanis, Rho meson distribution amplitudes from QCD sum rules with nonlocal condensates, Few Body Syst. **55**, 401 (2014).
[104] V. M. Braun *et al.* (QCDSF-UKQCD Collaboration), Distribution amplitudes of vector mesons, Proc. Sci. LATTICE2007 (**2007**) 144.
[105] R. Arthur, P. A. Boyle, D. Brömmel, M. A. Donnellan, J. M. Flynn, A. Jüttner, T. D. Rae, and C. T. C. Sachrajda (RBC and UKQCD Collaborations), Lattice results for low moments of light meson distribution amplitudes, Phys. Rev. D **83**, 074505 (2011).
[106] T. Zhong, Y.-H. Dai, and H.-B. Fu, $\rho$-meson longitudinal leading-twist distribution amplitude revisited and the $D \to \rho$ semileptonic decay, arXiv:2308.14032.
[107] R. G. Arnold, C. E. Carlson, and F. Gross, Elastic electron-deuteron scattering at high-energy, Phys. Rev. C **21**, 1426 (1980).
[108] H.-M. Choi and C.-R. Ji, Electromagnetic structure of the $\rho$ mesonin the light-front quark model, Phys. Rev. D **70**, 053015 (2004).
[109] F. Cardarelli, I. L. Grach, I. M. Narodetsky, G. Salme, and S. Simula, Electromagnetic form-factors of the rho meson in a light front constituent quark model, Phys. Lett. B **349**, 393 (1995).
[110] S. J. Brodsky and J. R. Hiller, Universal properties of the electromagnetic interactions of spin one systems, Phys. Rev. D **46**, 2141 (1992).
[111] W. Qian, S. Jia, Y. Li, and J. P. Vary, Light mesons within the basis light-front quantization framework, Phys. Rev. C **102**, 055207 (2020).
[112] M. Li, Y. Li, G. Chen, T. Lappi, and J. P. Vary, Light-front wavefunctions of mesons by design, Eur. Phys. J. C **82**, 1045 (2022).
[113] I. L. Grach and L. A. Kondratyuk, Electromagnetic form-factor of deuteron in relativistic dynamics. Two nucleon and six quark components, Sov. J. Nucl. Phys. **39**, 198 (1984), https://inspirehep.net/literature/191874.
[114] S. J. Brodsky and J. R. Hiller, Universal properties of the electromagnetic interactions of spin-one systems, Phys. Rev. D **46**, 2141 (1992).
[115] M. Gurtler *et al.* (QCDSF Collaboration), Vector meson electromagnetic form factors, *Proc. Sci.*, LATTICE2008 (2008) 051.
[116] C. J. Shultz, J. J. Dudek, and R. G. Edwards, Excited meson radiative transitions from lattice QCD using variationally optimized operators, Phys. Rev. D **91**, 114501 (2015).
[117] P. L. Chung, W. N. Polyzou, F. Coester, and B. D. Keister, Hamiltonian light front dynamics of elastic electron deuteron scattering, Phys. Rev. C **37**, 2000 (1988).
[118] M. S. Bhagwat and P. Maris, Vector meson form factors and their quark-mass dependence, Phys. Rev. C **77**, 025203 (2008).
[119] B. J. Owen, W. Kamleh, D. B. Leinweber, M. S. Mahbub, and B. J. Menadue, Light meson form factors at near physical masses, Phys. Rev. D **91**, 074503 (2015).
[120] M. E. Carrillo-Serrano, W. Bentz, I. C. Cloët, and A. W. Thomas, $\rho$ meson form factors in a confining Nambu–Jona-Lasinio model, Phys. Rev. C **92**, 015212 (2015).
[121] C. J. Shultz, J. J. Dudek, and R. G. Edwards (for the Hadron Spectrum Collaboration), Excited meson radiative transitions from lattice QCD using variationally optimized operators, Phys. Rev. D **91**, 114501 (2015).